Comparative assessment of linear least-squares, nonlinear least-squares, and Patlak graphical method for regional and local quantitative tracer kinetic modelling in cerebral dynamic ^{18}F-FDG PET

Fayçal Ben Bouallègue [1,2,(*)], Fabien Vauchot [1], Denis Mariano-Goulart [1,2]

(1) Department of Nuclear Medicine, Montpellier University Hospital, Montpellier, France

(2) PhyMedExp, INSERM, CNRS. Montpellier University. Montpellier, France

(*) corresponding author:

ABSTRACT

Purpose: Dynamic ^{18}F-FDG PET allows quantitative estimation of cerebral glucose metabolism both at the regional and local (voxel) level. Although sensitive to noise and highly computationally expensive, nonlinear least-squares (NLS) optimization stands as the reference approach for the estimation of the kinetic model parameters. Nevertheless, faster techniques, including linear least-squares (LLS) and Patlak graphical method, have been proposed to deal with high resolution noisy data, representing a more adaptable solution for routine clinical implementation. Former research investigating the relative performance of the available algorithms lack precise evaluation of kinetic parameter estimates under realistic acquisition conditions.

Methods: The present study aims at the systematic comparison of the feasibility and pertinence of kinetic modelling of dynamic cerebral ^{18}F-FDG PET using NLS, LLS, and Patlak method, based on numerical simulations and patient data. Numerical simulations were used to study K_1 and K_i parameters estimation bias and variance under representative noise levels. Patient data allowed to assess the concordance between the three methods at the regional and voxel scale, and to evaluate the robustness of the estimations with respect to patient head motion.

Results and Conclusions: Our findings indicate that at the regional level NLS and LLS provide kinetic parameter estimates (K_1 and K_i) with similar bias and variance characteristics (K_1bias ± rel. std dev. 0.0±5.1% and 0.1%±4.9% for NLS and LLS respectively, K_i bias ± rel. std dev. 0.1%±4.5% and -0.7%±4.4% for NLS and LLS respectively), NLS estimates being however slightly less sensitive to patient motion. At the voxel level, provided that patient motion is negligible or corrected, LLS offers an appealing alternative solution for local K_1 mapping, with high correlation with NLS values (Pearson's r = 0.95 on actual data) in computations times less than two orders of magnitude lower. Last, Patlak method appears as the most robust and accurate technique for the estimation of K_i values at the regional and voxel scale, with or without head motion. It provides low bias / low variance K_i quantification (bias ± rel. std dev. -1.5±9.5% and -4.1±19.7% for Patlak and NLS respectively) as well as smooth parametric images suitable for visual assessment.

Keywords: ^{18}F-FDG PET, cerebral glucose metabolism, quantification, kinetic analysis.

1. Introduction

Positron emission tomography (PET) allows absolute quantification of physiological parameters describing human brain function, such as cerebral blood flow using perfusion tracers (^{15}O-water), or cerebral glucose metabolism with ^{18}F-FDG [1-3]. However, since these parameters are not directly measurable, indirect parameter estimation based on activity measurements and kinetic modelling is required. The compartmental model for the determination of the local cerebral metabolic rate of glucose (CMRglu) was initially developed by Sokoloff and colleagues in the late 70's using ^{14}C-deoxy-glucose and an autoradiographic method [4], and further adapted to noninvasive assessment using ^{18}F-FDG PET [5]. Although simplified protocols relying on static scans combined with an assumption of fixed rate constants have been proposed for clinical routine implementation [6-7], dynamic data acquisition remains the state-of-the-art technique for complete and accurate kinetic parameter estimation [8-10]. Although original techniques based on machine learning have been proposed [11], iterative fitting of the compartment model and graphical approaches are most commonly employed to estimate the kinetic parameters.

Nonlinear least-squares (NLS) optimization stands as the reference technique for the estimation of the kinetic model parameters [12-13], based on the iterative minimization of an objective function to attain the best fitting of the model parameters to the measured PET data. The parameter estimates obtained using this method are expected to have optimal statistical accuracy [12]. Unfortunately, the least-squares objective function for multi-compartment models with noisy data is ill-formed, leading to results that are critically dependent upon parameter initialization [14-15]. Moreover, NLS optimization is highly demanding in terms of computational resources and thus of limited feasibility in parametric imaging, where voxel-wise computations are required.

Consequently, fast linear algorithms have been developed as an alternative to the nonlinear approach. Linear least-squares (LLS) and related generalized LLS methods involve a double integration of the modelling equations to obtain a linear system relating the rate parameters (or combinations thereof) to integrals of the tissue time-activity curve (TAC) and plasma input function [12, 16]. LLS is expected to provide parameter estimates that are highly correlated with those provided by NLS in a much shorter computation time. However, because the noise-related equation errors cannot be considered as independent random variables, bias may arise in parameter estimates when processing low count data such as voxel TACs [17].

The Patlak graphical method is a non-compartmental approach allowing a direct estimation of the metabolic rate of glucose without requiring the computation of the micro-parameters of the kinetic model [18]. It necessitates the computation of the slope of a transformed uptake curve that is supposed to exhibit a linear behaviour from about 15 minutes after tracer injection due to dominant unidirectional FDG transfer in steady-state conditions. The method is robust and computationally efficient [19-20] and has the potential to be compatible with multi-bed PET imaging [21]. However it does not allow for a complete description of the kinetic process, but only for an estimation of the net influx rate K_i.

Previous research reported on the comparative performance of the available algorithms for kinetic assessment of dynamic cerebral ^{18}F-FDG PET [12]. The authors performed a thorough evaluation of the available nonlinear, linear, and graphical methods, using numerical simulations and patient data. The study suffers however some limitations. In numerical simulations, a single set of kinetic parameters was employed, which did not allow to assess the correlation and concordance between parameter estimates and true values. The input function was assumed to be perfectly known and noiseless, which is not the case when exploiting an image-based vascular TAC [22-23], and the variability of input function shape that inherently affects clinical data was not accounted for. Further, the appropriateness of each method

in the particular cases of region of interest (ROI) modelling and voxel modelling was not evaluated, whether in numerical simulations or in patient data for which voxel-wise computations were not performed. Analogous evaluation of kinetic parameter estimation methods was reiterated more recently [24], anew based exclusively on numerical simulations using a single noiseless input function and a single set of reference kinetic parameters.

In the present study, starting from realistic numerical simulations, we evaluated the pertinence of NLS, LLS, and Patlak derived kinetic parameter estimates in terms of bias, variance, and concordance with ground-truth parameter values using vascular and tissue TACs corresponding to a variety of input functions and a range of kinetic parameter values. Noise level in both vascular and tissue TACs was tuned to fit with realistic image-based data for ROI and voxel modelling. The three methods were then tested using actual dynamic PET data from a healthy volunteer and compared on an ROI and voxel basis. Using these actual data, degraded images were simulated by convolution of a single time frame with a shifted 3D kernel, in order to assess the impact of patient head motion.

2. Methods

2.1. Theoretical background

Let us note $C_p(t)$ the time course of the arterial plasma concentration of ^{18}F-FDG and $C_c(t)$ the time course of the measurable ^{18}F-FDG concentration in the cerebral tissue compartment encompassing unmetabolized, metabolized, and vascular FDG. Let us note K_1, k_2, k_3, and k_4 the kinetic rate constants describing plasma-to-tissue exchange, tissue-to-plasma washout, phosphorylation, and dephosphorylation respectively, and β the relative blood volume (Figure 1).

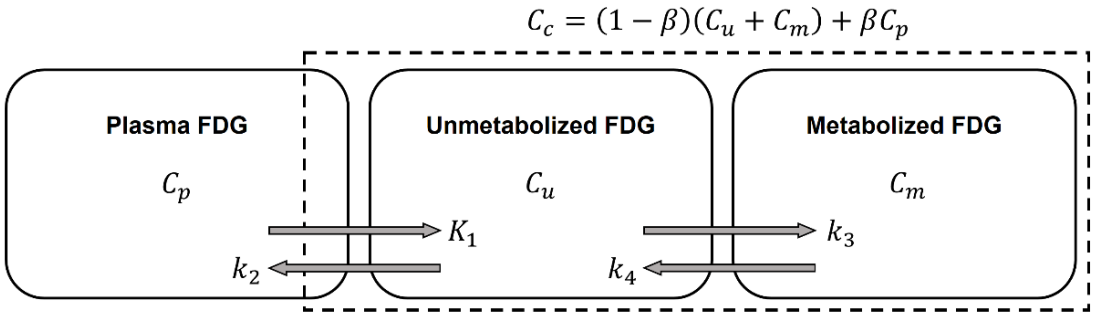

Fig. 1. Standard compartmental model used for ^{18}F-FDG kinetic modelling showing the PET measurments of plasma (C_p) and tissue (C_c) FDG concentrations, and the kinetic rate constants K_1, k_2, k_3, and k_4.

Considering that dephosphorylation of FDG is negligible in first approximation for short (< 60 min) scan duration [6, 8], one can derive the following differential equation governing the temporal evolution of $C_c(t)$[11]:

$$\frac{d^2}{dt^2}C_c(t) = -(k_2+k_3)\frac{d}{dt}C_c(t) + \beta\,\frac{d^2}{dt^2}C_p(t) + [\beta(k_2+k_3) + (1-\beta)K_1]\frac{d}{dt}C_p(t) + (1-\beta)K_1k_3C_p(t) \quad (1)$$

which closed-form solution is:

$$C_c(t) = (1-\beta)\left[\frac{K_1k_3}{k_2+k_3}\int_0^t C_p(\tau)d\tau + \frac{K_1k_2}{k_2+k_3}\int_0^t C_p(\tau)e^{-(k_2+k_3)(t-\tau)}d\tau\right] + \beta C_p(t) \quad (2)$$

The parameter

$$K_i = \frac{K_1 k_3}{k_2 + k_3} \tag{3}$$

is of foremost clinical relevance since it is directly related to the cerebral metabolic rate of glucose (*CMRglu*) according to $CMRglu = \frac{Gp}{LC} K_i$ with Gp denoting the plasma glucose concentration and LC the lumped constant describing the differential tissue avidity for glucose and FDG [6, 12]. As for the rate constant K_1, it may be thought of as a reflect of cerebral blood flow (*CBF*) since $K_1 = E.CBF$ with E denoting the extraction fraction of FDG. As FDG is not a perfect perfusion tracer, this relation is not linear due to the possible variation of the extraction fraction with the blood flow and underlying pathophysiological conditions.

Quantitative cerebral ^{18}F-FDG PET relies on dynamic data acquisition and image reconstruction over a sufficient time range starting from the injection of the tracer. The method allows to obtain image-based decay-corrected average measures of $C_p(t)$ and $C_c(t)$ on appropriately sampled time intervals of duration $\Delta_n$centred on t_n $(n = 1 \ldots \mathrm{N})$:

$$\overline{C_p}(t_n) = \frac{\int_{t_n - \Delta_n/2}^{t_n + \Delta_n/2} C_p(t)dt}{\Delta_n} \;;\; \overline{C_c}(t_n) = \frac{\int_{t_n - \Delta_n/2}^{t_n + \Delta_n/2} C_c(t)dt}{\Delta_n} \tag{4}$$

where $\overline{C_c}(t_n)$ may refer to either global, regional, or local (voxel-wise) tissue concentration.

2.1.1. Nonlinear least-squares

Based on the image-based measures, equation (2) may be rewritten as:

$$\overline{C_c}(t_n) = (1-\beta)\left(\frac{K_1 k_3}{k_2 + k_3}\left[\overline{C_p} * 1\right](t_n) + \frac{K_1 k_2}{k_2 + k_3}\left[\overline{C_p} * e^{-(k_2+k_3)t}\right](t_n)\right) + \beta\overline{C_p}(t_n) \tag{5}$$

where numerical convolution over the discrete sampling grid was defined as:

$$[\bar{C} * f(t)](t_n) = \sum_{i=1}^{i=n-1} \Delta_i \, \bar{C}(t_i) \, f(t_n - t_i) + \frac{\Delta_n}{2} \bar{C}(t_n) \, f\left(\frac{\Delta_n}{4}\right) \tag{6}$$

Equation (5) is a set of N nonlinear equations in the set of parameters $\{K_1, k_2, k_3, \beta\}$. Solving it in the sense of the least squares amounts to finding $\{K_1, k_2, k_3, \beta\}$ that minimize the L_2 norm of the difference between both sides of the equation over the N time points.

In the present study, NLS optimization was performed by means of the Levenberg-Marquardt algorithm [25] using the "MPfit" C subroutine library provided by the University of Wisconsin-Madison (https://www.physics.wisc.edu/~craigm/idl/cmpfit.html).

2.1.2 Linear least-squares

Integrating twice equation (1) with initial conditions $\frac{d}{dt}C_c(0) = \frac{d}{dt}C_p(0) = C_c(0) = C_p(0) = 0$ yields:

$$C_c(t) = -(k_2 + k_3)\int_0^t C_c(\tau)d\tau + \beta\, C_p(t) + \left[\beta(k_2 + k_3) + (1-\beta)K_1\right]\int_0^t C_p(\tau)d\tau +$$
$$(1-\beta)K_1 k_3 \iint_0^t C_p(\tau)d\tau \tag{7}$$

which can be rewritten based on the image-based measures as:

$$\overline{C_c}(t_n) = p_1[\overline{C_c} * 1](t_n) + p_2\,\overline{C_p}(t_n) + \; p_3\left[\overline{C_p} * 1\right](t_n) + \; p_4\left[\left[\overline{C_p} * 1\right] * 1\right](t_n) \tag{8}$$

Writing (8) for a sufficient number of values of t allows to build an over-determined linear system that can be expressed in matrix form:

$$\mathbf{A}\boldsymbol{p} = \boldsymbol{b}$$

with

$$\mathbf{A} = \begin{pmatrix} [\overline{C_c} * 1](t_1) & \overline{C_p}(t_1) & \left[\overline{C_p} * 1\right](t_1) & \left[\left[\overline{C_p} * 1\right] * 1\right](t_1) \\ \dots & & & \\ [\overline{C_c} * 1](t_{\mathrm{N}}) & \overline{C_p}(t_{\mathrm{N}}) & \left[\overline{C_p} * 1\right](t_{\mathrm{N}}) & \left[\left[\overline{C_p} * 1\right] * 1\right](t_{\mathrm{N}}) \end{pmatrix}$$

$$\boldsymbol{p} = (p_1, p_2, p_3, p_4)^{\mathrm{T}}$$

$$\boldsymbol{b} = \left(\overline{C_c}(t_1), \dots, \overline{C_c}(t_{\mathrm{N}})\right)^{\mathrm{T}} \tag{9}$$

and which solution in the sense of the least squares is:

$$\boldsymbol{p} = \left(\mathbf{A}^{\mathrm{T}}\mathbf{A}\right)^{-1}\mathbf{A}^{\mathrm{T}}\boldsymbol{b} \tag{10}$$

The kinetic parameters can then be recovered using:

$$\begin{cases} K_1 = \frac{p_1 p_2 + p_3}{1 - p_2} \\ k_2 = -p_1 - \frac{p_4}{p_1 p_2 + p_3} \\ k_3 = \frac{p_4}{p_1 p_2 + p_3} \\ \beta = p_2 \end{cases} \tag{11}$$

2.1.3. Patlak graphical method

For sufficiently large values of t, one can assume that steady-state conditions are reached (i.e., plasma and unmetabolized FDG have reached equilibrium) and that $e^{-(k_2+k_3)t}$ is negligible. In this case, and further hypothesizing that $\beta \sim 0$, equation (2) may be simplified to [26]:

$$C_c(t) = \frac{K_1 k_3}{k_2 + k_3}\int_0^t C_p(\tau)d\tau + \frac{K_1 k_2}{(k_2+k_3)^2}C_p(t) \tag{12}$$

Dividing through by $C_p(t)$ produces the Patlak graphical plot [18]:

$$\frac{C_c(t)}{C_p(t)} = K_i\frac{\int_0^t C_p(\tau)d\tau}{C_p(t)} + \frac{K_1 k_2}{(k_2+k_3)^2} \tag{13}$$

Writing (13) for a sufficient number of values of t using image-based measures allows to estimate the slope of the Patlak plot K_i using linear regression. Contrary to linear and nonlinear least-squares, the micro-parameters K_1, k_2, and k_3 cannot be estimated using Patlak method.

2.2. Numerical simulations

Numerical simulations were run using vascular input functions expressed as the sum of a gamma variate modelling the peak and two decreasing exponentials modelling recirculation [12, 24, 27, 28]:

$$C_p(t) = \; [A_1(t - t_0)^{\alpha} - A_2 - A_3]e^{-\lambda_1(t-t_0)} + A_2 e^{-\lambda_2(t-t_0)} + A_3 e^{-\lambda_3(t-t_0)} \tag{14}$$

with the shape parameters randomly generated (uniform distribution) in the range $A_1 \in [600-1000]$, $\alpha \in [0.8-1.2]$, $\lambda_1 \in [3-5]$, $A_2 \in [10-30]$, $\lambda_2 \in [0.01-0.02]$, $A_3 \in [10-30]$, $\lambda_3 \in [0.1-0.2]$, and t_0 set to 1 min [28].Values of $C_p(t)$ were computed on a fine time grid with a constant sampling step of 500 ms.

Tissue uptake $C_c(t)$ was then numerically computed using equation (2) with randomly generated values (uniform distribution) of the kinetic parameters in the range [2, 10, 29-31] $K_i \in [0.02-0.05]$, $K_1 \in [0.07-0.13]$, $k_2 \in [0.06-0.20]$, and $\beta \in [1\%-5\%]$, and k_3 constrained by $\left\{k_3 = \frac{k_2 K_i}{K_1 - K_i};\ k_3 \leq 0.15\right\}$.

Discrete image-based measures of vascular and tissue TACs were simulated using equation (4) and the following sampling scheme corresponding to a total 40 minute scan duration:

$$\Delta_n = \{12 \times 10s\ ;\ 6 \times 30s; 5 \times 60s; 6 \times 300s\} \tag{15}$$

In addition to the ideal TACs derived from equation (4), realistic noisy TACs were produced using a pseudo-random number generator following [12, 24, 32]:

$$\begin{cases} \overline{C_p}(t_n) \sim G\left(\frac{\int_{t_n-\Delta_n/2}^{t_n+\Delta_n/2} C_p(t)dt}{\Delta_n}\ ,\eta\sqrt{\frac{\int_{t_n-\Delta_n/2}^{t_n+\Delta_n/2} C_p(t)dt}{\Delta_n}}\right) \\ \overline{C_c}(t_n) \sim G\left(\frac{\int_{t_n-\Delta_n/2}^{t_n+\Delta_n/2} C_c(t)dt}{\Delta_n}\ ,\eta\sqrt{\frac{\int_{t_n-\Delta_n/2}^{t_n+\Delta_n/2} C_c(t)dt}{\Delta_n}}\right) \end{cases} \tag{16}$$

with $G(\mu, \sigma)$ the Gaussian distribution of mean μ and standard deviation σ.

The parameter η was empirically determined so as to comply with the observed noise levels in actual dynamic PET data acquired at our institution, and to achieve similar goodness of fit in terms of model root-mean-square error (RMSE). It was set to 1.6 for the vascular TAC, while it was set either to 0.6 or 2.8 for the tissue TAC so as to emulate TACs describing large cortical ROIs or single voxels respectively. For illustration purposes, Figure 2 shows representative exact and sampled vascular and tissue TACs.

For each noise level (ideal TACs, noisy vascular TAC with ROI tissue TAC, noisy vascular TAC with voxel tissue TAC), 1000 simulations were conducted, each simulation corresponding to a randomly generated set of input function shape parameters and kinetic constants. For NLS and LLS, the goodness of fit was quantified using the relative RMSE between the simulated tissue TAC and the kinetic fit provided by the method. The quality of the kinetic constant estimations (K_1, k_2, k_3, and K_i) was assessed through their relative bias and variance, and through their correlation (Pearson's coefficient) and concordance (Lin's coefficient) with the true values.

Given a set of pairs $\{x_i; \bar{x}_i\}$ with x_i denoting the parameter estimates, $\bar{x}_i$ the true parameter values, and $E[\cdot]$ the statistical expected value. The relative bias b, mean square relative error ε, and relative standard deviation σ were computed as:

$$b = E\left[\frac{x_i - \bar{x}_i}{\bar{x}_i}\right]$$

$$\varepsilon = \sqrt{E\left[\left(\frac{x_i - \bar{x}_i}{\bar{x}_i}\right)^2\right]}$$

$$\sigma = \sqrt{\varepsilon^2 - b^2} \tag{17}$$

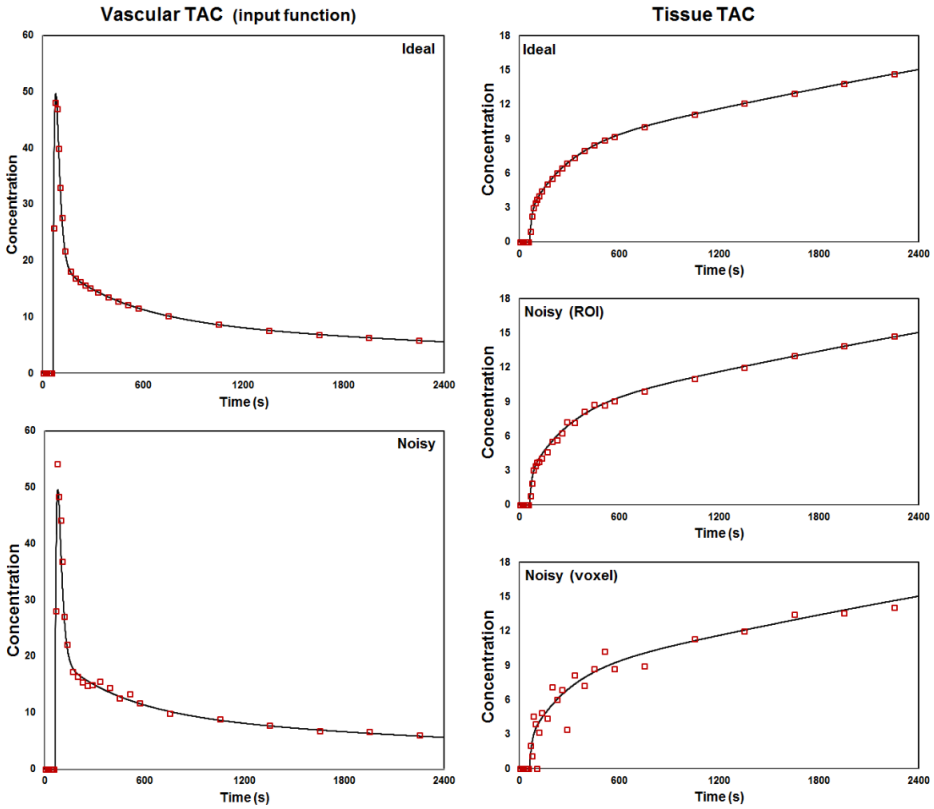

Fig. 2. Representative exact (plain line) and sampled (square markers) vascular and tissue time-activity curves (TAC) used for numerical simulations. Concentration in arbitrary units. Parameters were set at their median value (input function: A_1=400; λ_1=4; A_2=10; λ_2=0.15; A_3=10; λ_3=0.015; α =1; tissue: K_1=0.10; k_2=0.13; k_3=0.07; K_i=0.035; β =3%).

Using NLS and LLS, parameter estimates were constrained within the following bounds that were chosen wide enough to encompass the documented parameter values in grey and white matter [2, 10, 29-31]: $0 \leq K_1 \leq 0.25$, $0 \leq k_2 \leq 0.30$, $0 \leq k_3 \leq 0.20$, and $0\% \leq \beta \leq 10\%$. Regarding NLS, the Levenberg-Marquardt algorithm was initialized using the median values of the randomly generated kinetic parameters, so as to minimize the computation time and avoid inducing artefactual algorithm failure due to inappropriate initialization. As for Patlak method, the evaluation of the linear regression slope was performed based either on the 4 last time points (25–40 min) or 6 last time points (15–40 min).

2.3. Actual dynamic PET data

A dynamic cerebral PET study was realized in a healthy 27 year-old male volunteer after a fasting period of 8 hours. The examinations was performed using a time-of-flight Siemens Biograph mCT Flow scanner [33] following IV injection of 2.5 MBq/Kg of ^{18}F-FDG for a total duration of 40 minutes. Dynamic frames corresponding to the time sampling described in equation (15) were reconstructed using 3D OSEM (21 subsets and 2 iterations, including PSF correction) followed by a 5mm Gaussian post-filtering.

The last time frame (35-40 minutes) was spatially normalized to the standard Montreal Neurological Institute (MNI) space using SPM12 (Wellcome Trust Centre, London, UK). Preceding frames were normalized using the same transformation. Resulting PET data were sampled on a 135×155×128 grid

with cubic voxels of 1.5×1.5×1.5 mm^3. PET image voxels were labeled according to the maximum probability tissue atlas derived from the "MICCAI 2012 grand challenge and workshop on multi-atlas labeling" and provided by Neuromorphometrics, Inc. (neuromorphometrics.com) under academic subscription, allowing to define the following cortical ROIs: frontal, temporal, parietal, occipital, insula, cingulum, and precuneus.

A 3×3×3 voxel vascular ROI was placed on each internal carotid artery in its petrous portion. The vascular input function was computed by extracting the TACs inside these two ROIs, averaging them, and correcting for partial volume effect and spillover using a recovery coefficient of 40%[1]. Vascular ROI placement was automated so as to maximize the TAC peak.

Kinetic parameters (K_1, k_2, k_3, and/or K_i) were estimated in each cortical ROI and on a voxel basis using the 3 aforementioned algorithms. Using NLS and LLS, parameter estimates were constrained within the bounds specified in the previous section. Patlak plot linear regression was performed using the 6 last time points (15–40 min). Voxel $K_1$and K_i estimates were compared between methods using Pearson's correlation and Lin's concordance.

In order to assess algorithm sensitivity to patient motion, the same computations were renewed after having numerically altered one time frame in order to simulate head motion. Ten sec frames 7 to 12 (60–120 sec) were used to simulate early motion during tracer first pass, and 5 min frames 24 to 29 (10–40 min) were used to simulate late motion during cerebral uptake (see Figure 3). Image offset and blurring resulting from head motion was simulated by convolving the considered frame with a shifted 3D kernel centred (in mm) on $(\Delta x, \Delta y, \Delta z) \in \{-1.5, 0, 1.5\}^3$, resulting in 162 (6 time frames × 27 kernel positions) early and 162 late motion simulations.

The kernel was defined on a 3×3×3 voxel grid as:

$$\kappa(x, y, z) = \frac{1}{1+\gamma\sqrt{x^2+y^2+z^2}} \tag{17}$$

The weighting coefficient γ was set to 1 when simulating early motion and 2 when simulating late motion (these values were set empirically in order to induce a relative variability of about 3% in whole-cortex NLS K_i estimates).

When assessing voxel-wise parameter estimates, due to computation burden considerations, motion simulations were restricted to $(\Delta x, \Delta y, \Delta z) \in \{(\pm 1.5,0,0); (0, \pm 1.5,0); (0,0, \pm 1.5)\}$, resulting in 36 (6 time frames × 6 kernel positions) early and 36 late motion simulations.

Robustness of regional parameter estimates (K_1 and K_i) was assessed through their relative bias and standard deviation with respect to motion-less parameter value. Robustness of voxel parametric K_1 and K_i maps was evaluated by computing for each motion simulation the normalized L_2 norm of the difference between the parametric map in motion condition and the reference map without motion (normalization was performed with respect to average map value) and by comparing the distribution of difference map L_2 norm between algorithms using Student's t-test.

[1] The recovery coefficient was computed numerically based on the geometrical assumption of a cylindrical carotid artery of 5 mm diameter [34] and a spatial resolution of 6.25 mm (3.8 mm intrinsic resolution and 5 mm post-smoothing).

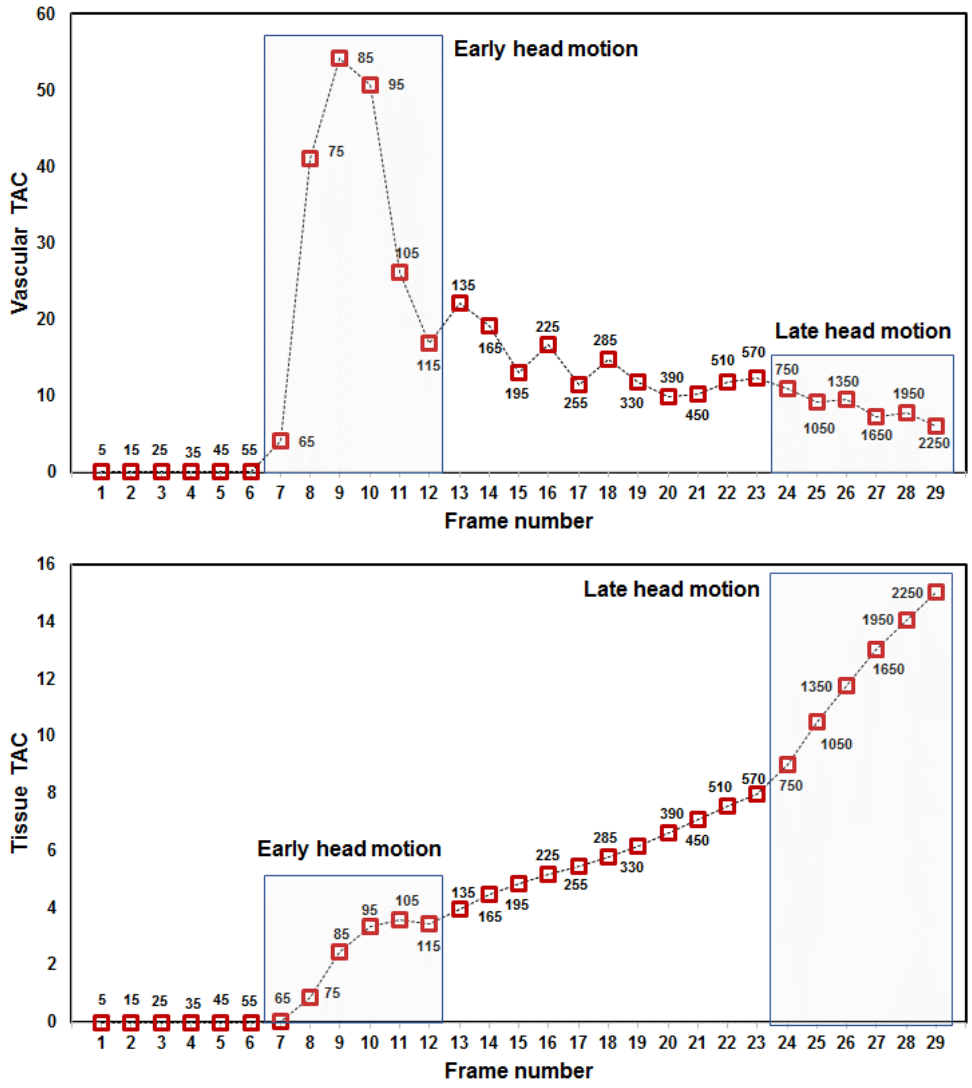

Fig. 3. Vascular (top) and whole cortex tissue (bottom) TACs from actual dynamic PET data showing the 6 early and 6 late time frames in which patient head motion was simulated. Note that the abscissa are labelled according to frame number. The small tags indicate (in seconds) the centre of each time interval over which the TACs have been measured.

3. Results

3.1. Numerical simulations

Table 1 summarizes the results of the three methods in terms of goodness of fit and quality of kinetic parameter estimates for each of the three noise levels.

Regarding K_1, NLS and LLS provided very low bias (0–2%) estimates regardless of the noise level. Concordance with true K_1 values was almost perfect using ideal and ROI TACs (Lin's coefficient above 0.95), whereas it substantially decreased at voxel noise (Lin's coefficient ~ 0.65–0.70). Besides, NLS and LLS K_1 estimates had very similar characteristics across the simulated noise range.

Regarding K_i, NLS and LLS estimates were of identical quality and highly concordant with true values in case of ideal and ROI TACs (Lin's coefficient ~ 1). Using voxel TACs, NLS and LLS bias and variance tended to substantially increase, leading to moderate concordance with true values (Lin's coefficient ~ 0.70–0.80). On the contrary, Patlak estimates (6 points) showed minimal bias below 2%

regardless of the noise level (vs <1% for ideal and ROI TACs and 4–7% for voxel TACs using least-squares methods). Patlak estimates exhibited a slowly growing variance around 7–9% (vs <1%, ~5%, and ~20% for ideal, ROI, and voxel TACs respectively, using least-squares methods), which allowed to maintain high concordance with true values even using voxel TACs (Lin ~ 0.95).

Figure 4 shows the distribution of the relative error in K_1 (left) and K_i (right) estimates according to true parameter values. Distributions were quite identical using NLS and LLS, with a dispersion that substantially increased when passing from ROI noise to voxel noise. The slowly growing dispersion of Patlak K_i estimates with noise level that was evidenced in Table 1 is clearly apparent in the Figure.

3.2. Actual dynamic PET data

Figure 5 shows the histograms of regional K_1 (A) and K_i (B) estimates. Mean model RMSE over the 14 cortical ROIs was 3.3% for NLS and 3.4% for LLS. Mean relative difference between LLS and NLS was -1.7% for K_1 and -1.5% for K_i. Mean K_i relative difference was -1.8% and -0.4% between Patlak and NLS, and Patlak and LLS respectively.

Figure 6 shows the scatter plots of the kinetic parameters computed on a voxel basis inside the cortical area, the 14 cortical ROIs gathering a total of 241,465 voxels. Correlation was excellent between LLS and NLS K_1 estimates (subplots A; Pearson's r = 0.95) and K_i estimates (subplots B; Pearson's r = 0.97), and between Patlak and NLS K_i estimates (subplots C; Pearson's r = 0.95). Mean model RMSE over the cortical voxels was 15.4% for NLS and 16.1% for LLS. Figure 7 shows representative axial slices of K_1 (top) and K_i (bottom) voxel parametric maps obtained using the three tested methods.

Figure 8 shows the relative bias ± standard deviation of regional K_1 and K_i estimates obtained using the three tested algorithms based on altered PET data with simulated early (top) and late (bottom) head motion. Early/late bias ± standard deviation for whole-cortex estimates was 2.8±4.6%/0.1±1.9% and 1.9±5.7%/-0.2±2.7% for NLS and LLS K_1 estimates respectively, and 0.5±3.1%/1.6±3.0%, 0.4±3.1%/1.5±3.1%, and -0.3±3.2%/1.5±2.9% regarding NLS, LLS, and Patlak K_i estimates respectively.

Figure 9 shows the distribution of the difference map L_2 norm in condition of early (top) and late (bottom) head motion. In late motion simulations, LLS K_1 and K_i estimates were significantly more prone to variation than NLS estimates. Patlak K_i estimates were significantly more robust than NLS estimates in both early and late motion simulations.

Table 2 provides indicative computation times for the three studied methods. There was an approximate 20-fold increase in computation burden between Patlak and LLS, and a 250-fold increase between LLS and NLS.

Table 1

Performance of nonlinear least-squares (NLS), linear least-squares (LLS), and Patlak graphical method in numerical simulations. For each noise level (ideal, ROI, and voxel, see text for details), each algorithm was run 1000 times using randomly generated input functions and tissue parameters (see text for details). SD: standard deviation. Pearson: Pearson's correlation. Lin: Lin's concordance. Patlak (4) and (6) refer to the number of time points used to compute the Patlak plot regression.

	Mean model	K_1				k_2				k_3				K_i			
	RMSE	Bias	SD	Pearson	Lin	Bias	SD	Pearson	Lin	Bias	SD	Pearson	Lin	Bias	SD	Pearson	Lin
Ideal																	
NLS	0.3%	-0.2%	0.3%	1	1	-1.5%	0.9%	1	1	-0.3%	1.0%	1	1	0.6%	0.5%	1	1
LLS	0.3%	0.1%	0.1%	1	1	-0.2%	0.6%	1	1	-0.5%	0.7%	1	1	-0.1%	0.3%	1	1
Patlak (4)	–	–	–	–	–	–	–	–	–	–	–	–	–	-4.0%	3.4%	0.99	0.98
Patlak (6)	–	–	–	–	–	–	–	–	–	–	–	–	–	-1.4%	6.7%	0.97	0.97
Noisy (ROI)																	
NLS	3.6%	0.0%	5.1%	0.96	0.96	-0.9%	14.4%	0.92	0.92	-0.7%	12.5%	0.97	0.97	0.1%	4.5%	0.99	0.99
LLS	3.7%	0.1%	4.9%	0.96	0.96	-0.6%	13.2%	0.91	0.90	-1.7%	11.4%	0.96	0.96	-0.7%	4.4%	0.99	0.99
Patlak (4)	–	–	–	–	–	–	–	–	–	–	–	–	–	-3.7%	5.8%	0.98	0.97
Patlak (6)	–	–	–	–	–	–	–	–	–	–	–	–	–	-0.9%	7.2%	0.97	0.97
Noisy (voxel)																	
NLS	16.1%	1.3%	16.6%	0.70	0.66	6.7%	55.7%	0.55	0.46	-0.8%	45.1%	0.69	0.66	-4.1%	19.7%	0.81	0.78
LLS	16.4%	-2.1%	16.5%	0.72	0.67	-7.3%	41.8%	0.49	0.41	-12.2%	37.9%	0.65	0.62	-7.3%	22.0%	0.74	0.69
Patlak (4)	–	–	–	–	–	–	–	–	–	–	–	–	–	-3.9%	15.1%	0.85	0.84
Patlak (6)	–	–	–	–	–	–	–	–	–	–	–	–	–	-1.5%	9.5%	0.94	0.94

Table 2

Indicative computation times using a 2×2.40 GHz processor for nonlinear least-squares (NLS), linear least-squares (LLS), and Patlak graphical method.

	One run	**Actual PET data (250,000 cortical voxels)**
NLS	2 ms	8 min
LLS	8 μs	2 s
Patlak	0.4 μs	100 ms

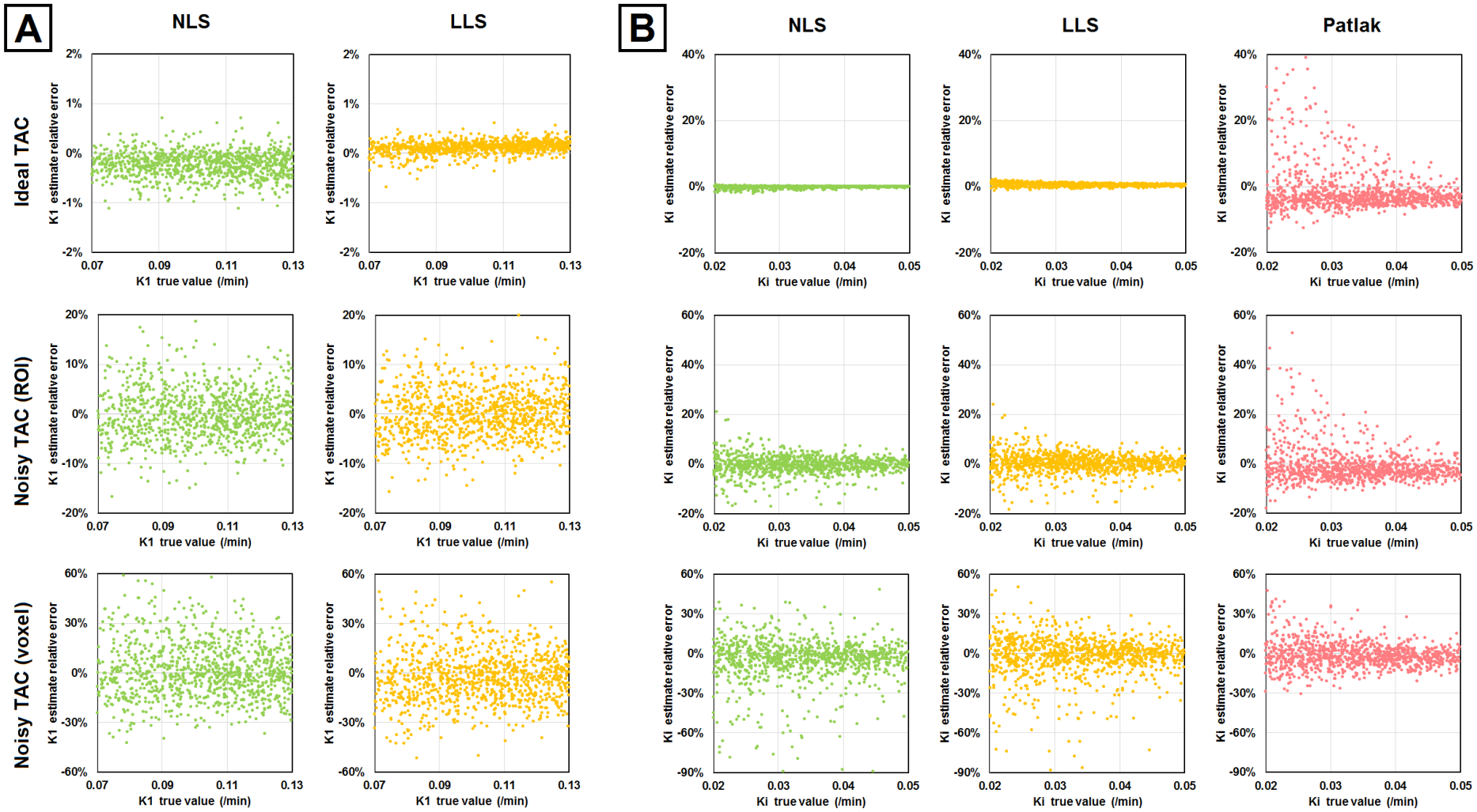

Fig. 4. Scatter plots of the relative error in K_1 (A) and K_i (B) estimates obtained using nonlinear least-squares (NLS), linear least-squares (LLS), and Patlak graphical method (6 time points) in numerical simulations. For each noise level (ideal, ROI, and voxel, see text for details), each algorithm was run 1000 times using randomly generated input functions and tissue parameters (see text for details). Mind that the ordinate scale is variable.

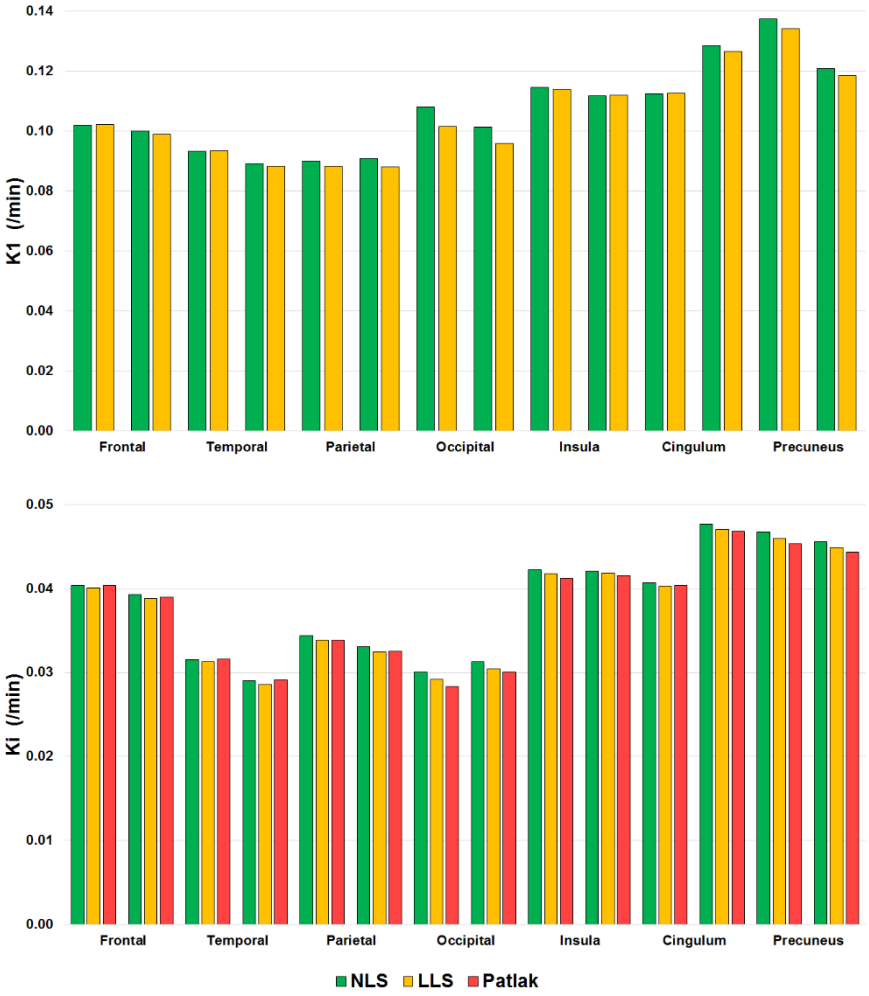

Fig. 5. Regional cortical K_1 (top) and K_i (bottom) values obtained using nonlinear least-squares (NLS), linear least-squares (LLS), and Patlak graphical method based on actual dynamic PET data. Each cortical ROI is divided into left then right, except the cingular cortex which is divided into anterior then posterior.

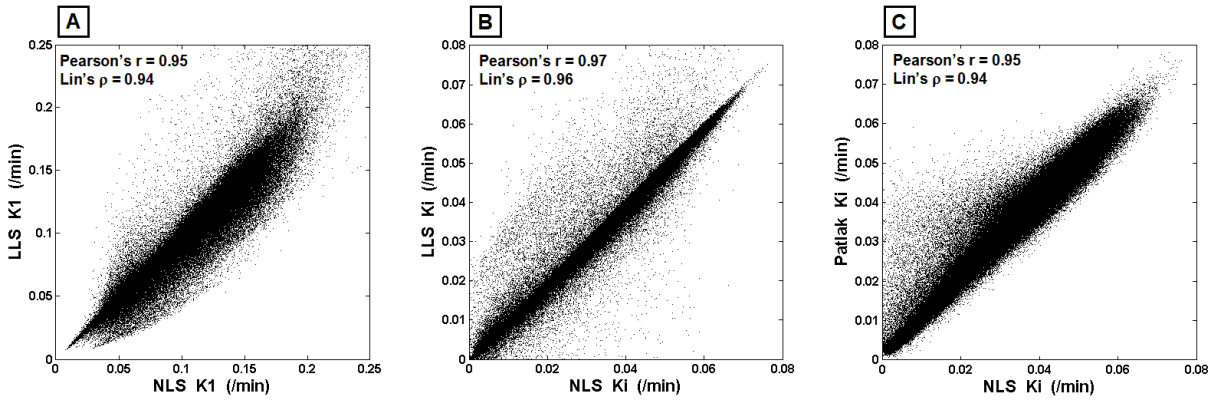

Fig. 6. Scatter plots of cortical voxel K_1 and K_i values obtained using nonlinear least-squares (NLS), linear least-squares (LLS), and Patlak graphical method based on actual dynamic PET data. (A): LLS vs NLS K_1; (B): LLS vs NLS K_i; (C): Patlak vs NLS K_i.

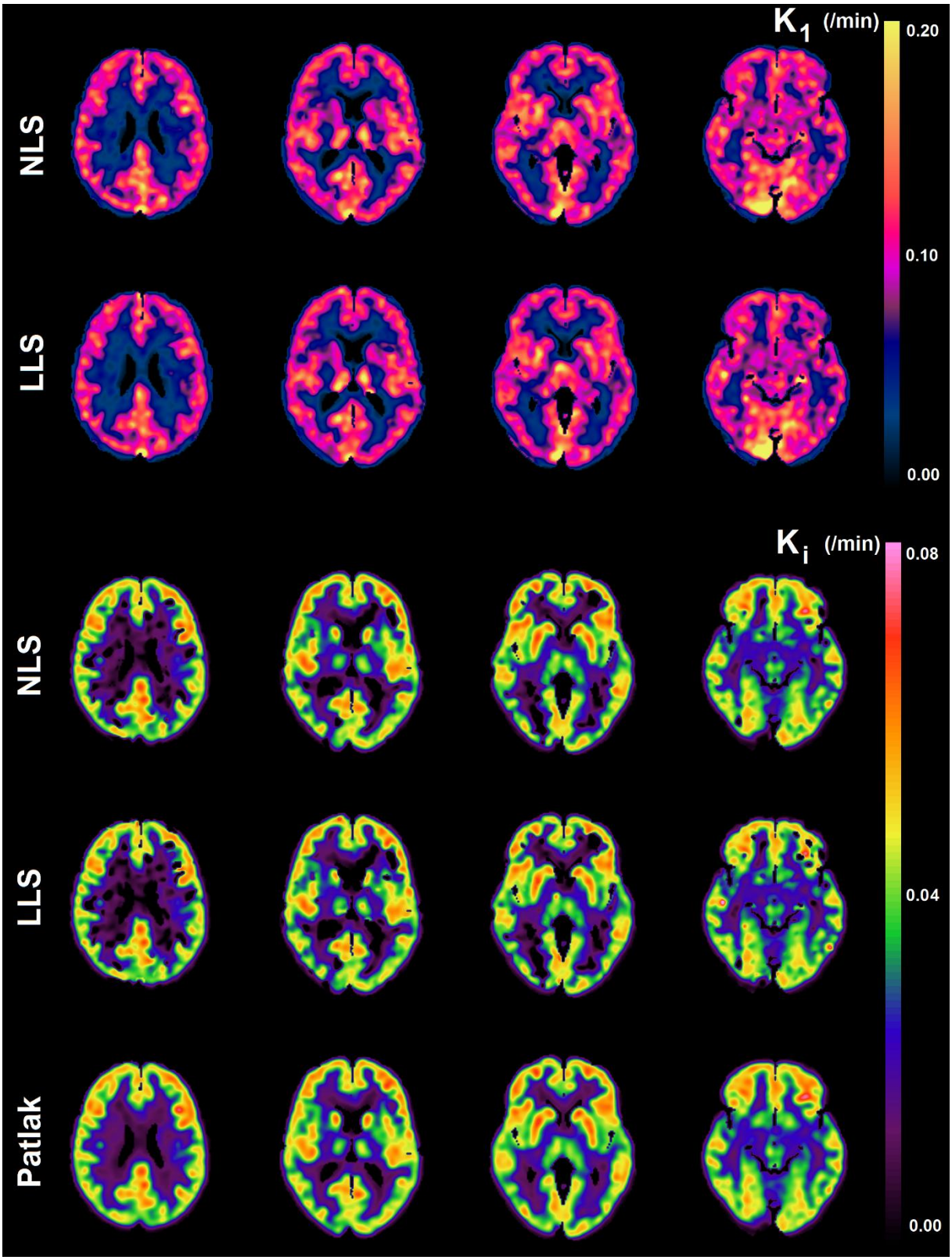

Fig. 7. K_1 (top) and K_i (bottom) parametric maps obtained using nonlinear least-squares (NLS), linear least-squares (LLS), and Patlak graphical method based on actual dynamic PET data.

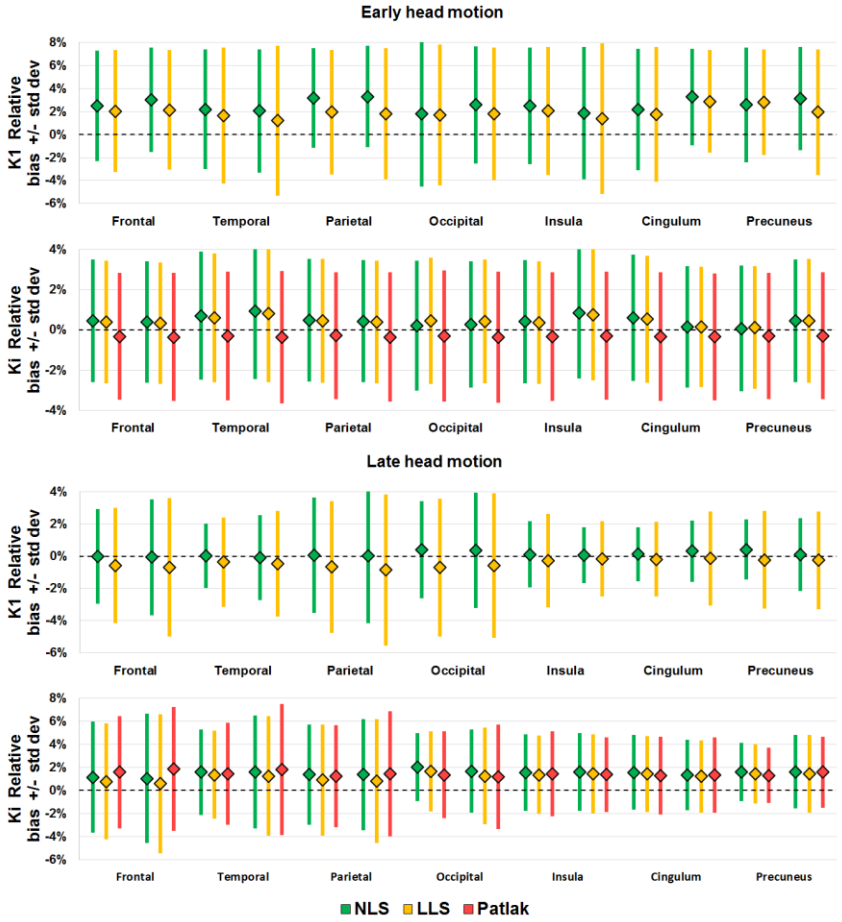

Fig. 8. Relative bias ± standard deviation (with respect to motion-less parameter values) in regional K_1 and K_i estimates obtained using nonlinear least-squares (NLS), linear least-squares (LLS), and Patlak graphical method based on actual dynamic PET data with simulated early (top) and late (bottom) head motion. Each cortical ROI is divided into left then right, except the cingular cortex which is divided into anterior then posterior.

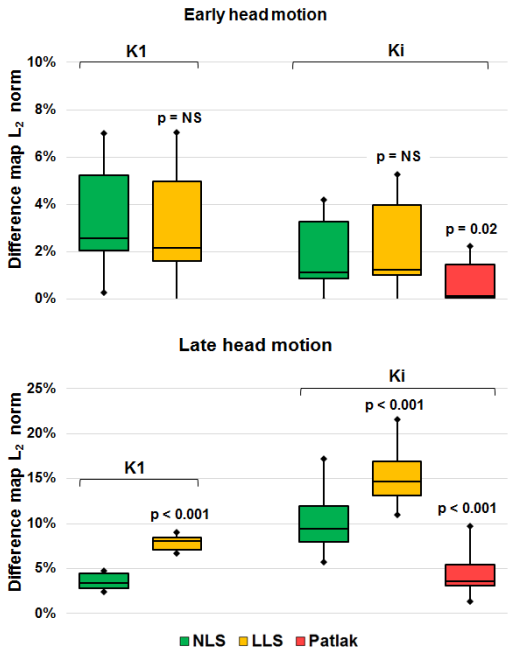

Fig. 9. Normalized L_2 norm of the difference between the voxel parametric maps obtained with and without motion simulation. Boxes: median and interquartile range; whiskers: mean ± standard deviation. Given p-values are with respect to NLS.

4. Discussion

Accurate and robust analysis of dynamic PET data using complete kinetic modelling is essential to obtain reliable estimations of physiological parameters such as cerebral blood flow and cerebral metabolic rate of glucose. On the other hand, the high dimensionality of dynamic measurements requires the development of fast analysis techniques compatible with routine exploitation.

In the present study, we deliberately chose to focus on NLS and LLS as the reference nonlinear and linear approaches respectively, since the added value of more elaborated optimization schemes (weighted least-squares, generalized least-squares, basis functions, ridge regression) remains controversial in the context of ^{18}F-FDG kinetic modelling [12, 24]. Our goal was to determine to what extent fast algorithms such as LLS and Patlak graphical method were suitable for glucose metabolism assessment at the ROI and voxel level in routine clinical conditions with comparison to the reference NLS method.

In numerical simulations, the range of variation of the kinetic parameters K_1, k_2, and K_i was selected based on previously documented values in healthy subjects [2, 10, 29-30]. FDG dephosphorylation was considered negligible, which was motivated by the fact that normal values of the dephosphorylation rate k_4 are very low compared to the other kinetic constants (0.005 to 0.01/min) [6, 29]. Using short scan durations (less than 60 minutes), estimations of k_4 are hence expected to be unreliable and of little relevance [8, 35], and minimal errors induced by the approximation k_4=0 are expected to have a negligible impact on K_i quantification [36]. It has however to be noted that non-negligible k_4 values may be observed, in particular in neoplastic tissues [37]. In that particular case, a potential solution lies in the use of generalized Patlak model which is non-linear but sufficiently robust to be applied in clinical routine oncological imaging [38].

Our study specifically centred on the ability of the tested algorithms to provide reliable estimates of K_1 and K_i, since these two parameters are of clinical relevance in brain PET, the first correlating with cerebral perfusion and the latter quantifying glucose metabolism. Indeed, there is no consensual pathophysiological, let alone clinical, interpretation of variations in k_2 or k_3 micro-parameters. Thus, their estimation can be considered as less critical, compared to K_1 and K_i, when performing kinetic modelling or related parametric imaging methods.

Our actual dynamic PET data were used to simulate patient motion during acquisition and evaluate its impact on parameter estimation. Because of the long duration of the scanning protocol, dynamic PET data are expected to be affected by head motion, particularly during the last time frames due to patient discomfort. Motions in the millimetre range were simulated because larger image shift should be more easily observed in the acquired data and subsequently corrected using image registration methods. Although less likely in clinical setting, early head motion was also simulated owing to its potential incidence on input function measurement.

The results presented in the previous section highlight that the algorithmic approach should be tailored to the desired modelling scale and decided according to the computing power at hand. This last consideration appears particularly critical insofar as the performance of the different methods seem rather similar while their computational burden largely differ.

When the focus in on regional kinetic modelling in large cortical ROIs, the results indicate that NLS optimization provides the best parameter estimates in reasonable computation time, with negligible bias, minimal variance, and almost perfect concordance with true parameter values. Using actual data with simulated head motion, NLS K_1 estimates were clearly less sensitive to transient image misregistration

than LLS estimates. No substantial difference was found between the three methods in terms of regional K_i estimates under both early and late motion conditions.

K_1 parametric mapping requires a complete kinetic modelling and the processing of high-dimensional dynamic data at the voxel level. In this frame, LLS optimization may stand as a well-grounded alternative to NLS for the estimation of the K_1 parametric map. Numerical simulations demonstrated an equal performance for the two methods in terms of bias, variance, and concordance with ground-truth parameter value. Using actual data, NLS and LLS K_1 values were highly correlated (Pearson's r = 0.95), yielding visually identical parametric images (Figure 7, top). However, LLS showed more sensitivity to head motion during the late time frames than NLS did (about 8% vs 4% relative error). This was likely due to the fact that, contrary to NLS, the integration scheme involved in LLS increases its sensitivity to data inaccuracies occurring at later time frames. NLS modelling should hence be preferred whenever late head motion is observed and accurate co-registration is not available or not feasible.

When K_i parametric mapping is desired, Patlak graphical method appears both as the fastest and most reliable method. In numerical simulations using voxel noise, it achieved the lowest bias and variance, and highest concordance with true K_i values, while using actual data it provided K_i estimates highly correlated with NLS estimates (Pearson's r = 0.95). The low variance exhibited in numerical simulations translated visually in the parametric images (Figure 7, bottom) which appeared more suitable for qualitative assessment than NLS and LLS derived images. Patlak method also provided K_i maps that were significantly less sensitive to patient motion than NLS and LLS maps, whether in early or late head motion simulations. This low sensitivity to data inconsistencies may be explained by the robustness of the linear regression over 6 late time points, and by the fact that errors in the input function peak are expected to have little influence on its area under the curve. Beyond the scope of the present study, another advantage of the Patlak method lies in its compatibility with multi-bed imaging, allowing for whole-body parametric imaging in clinical oncology [39].

5. Conclusions

Based on realistic numerical simulations as well as actual patient data, the present study stresses the need for an appropriate algorithmic approach according to the desired parametric modelling and the data dimensionality. When working with low-noise low-dimension data (regional assessment), NLS stands as the reference method for K_1 and K_i estimation. When analysing high-noise high-dimension data (local/voxel assessment), due to computation time considerations, LLS appears as a reasonable alternative to NLS for K_1 estimation, if a complete solution of the kinetic model is desired (for instance in order to estimate local K_1 as a surrogate to blood flow). When the focus is on the estimation of K_i as an indicator of glucose metabolism, Patlak graphical method achieves the lowest bias, variance, and sensitivity to patient motion. Its higher robustness translates into parametric images with suitable smoothness for visual assessment. Thus the Patlak method should be preferred over complete kinetic modelling for voxel-wise K_i mapping.

Disclosure of Conflicts of Interest

The authors have no relevant conflicts of interest to disclose.

References

1. Chen K, Bandy D, Reiman E, et al. Noninvasive quantification of the cerebral metabolic rate for glucose using positron emission tomography, 18F-fluoro-2-deoxyglucose, the Patlak method, and an image-derived input function. J Cereb Blood Flow Metab. 1998;18(7):716-23.

2. Reivich M, Alavi A, Wolf A, et al. Glucose metabolic rate kinetic model parameter determination in humans: the lumped constants and rate constants for [18F]fluorodeoxyglucose and [11C]deoxyglucose. J Cereb Blood Flow Metab. 1985;5(2):179-92.

3. Alpert N. Optimization of regional cerebral blood flow measurements with PET. J Nucl Med. 1991;32(10):1934-6.

4. Sokoloff L, Reivich M, Kennedy C, et al. The [14C]deoxyglucose method for the measurement of local cerebral glucose utilization: theory, procedure, and normal values in the conscious and anesthetized albino rat. J Neurochem. 1977;28(5):897-916.

5. Reivich M, Kuhl D, Wolf A, et al. The [18F]fluorodeoxyglucose method for the measurement of local cerebral glucose utilization in man. Circ Res. 1979;44(1):127-37.

6. Phelps ME, Huang SC, Hoffman EJ, Selin C, Sokoloff L, Kuhl DE. Tomographic measurement of local cerebral glucose metabolic rate in humans with (F-18)2-fluoro-2-deoxy-D-glucose: validation of method. Ann Neurol. 1979;6(5):371-88.

7. Wienhard K, Pawlik G, Herholz K, Wagner R, Heiss WD. Estimation of local cerebral glucose utilization by positron emission tomography of [18F]2-fluoro-2-deoxy-D-glucose: a critical appraisal of optimization procedures. J Cereb Blood Flow Metab. 1985;5(1):115-25.

8. Heiss WD, Pawlik G, Herholz K, Wagner R, Göldner H, Wienhard K. Regional kinetic constants and cerebral metabolic rate for glucose in normal human volunteers determined by dynamic positron emission tomography of [18F]-2-fluoro-2-deoxy-D-glucose. J Cereb Blood Flow Metab. 1984;4(2):212-

9. Piert M, Koeppe RA, Giordani B, Berent S, Kuhl DE. Diminished glucose transport and phosphorylation in Alzheimer's disease determined by dynamic FDG-PET. J Nucl Med. 1996;37(2):201-8.

10. Huisman MC, van Golen LW, Hoetjes NJ, et al. Cerebral blood flow and glucose metabolism in healthy volunteers measured using a high-resolution PET scanner. EJNMMI Res. 2012;2(1):63.

11. Pan L, Cheng C, Haberkorn U, Dimitrakopoulou-Strauss A. Machine learning-based kinetic modeling: a robust and reproducible solution for quantitative analysis of dynamic PET data. Phys Med Biol. 2017;62(9):3566-3581.

12. Feng D, Ho D, Chen K, et al. An evaluation of the algorithms for determining local cerebral metabolic rates of glucose using positron emission tomography dynamic data. IEEE Trans Med Imaging. 1995;14(4):697-710.

13. O'Sullivan F, Saha A. Use of ridge regression for improved estimation of kinetic constants from PET data. IEEE Trans Med Imaging. 1999;18(2):115-25.

14. Zeng GL, Hernandez A, Kadrmas DJ, Gullberg GT. Kinetic parameter estimation using a closed-form expression via integration by parts. Phys Med Biol. 2012;57(18):5809-21.

15. Ikoma Y, Watabe H, Shidahara M, Naganawa M, Kimura Y. PET kinetic analysis: error consideration of quantitative analysis in dynamic studies. Ann Nucl Med. 2008;22(1):1-11

16. Evans AC. A double integral form of the three-compartmental, four-rate-constant model for faster generation of parameter maps. J Cereb Blood Flow Metab 1987; 7 (Suppl 1): S453.

17. Cai W, Feng D, Fulton R, Siu WC. Generalized linear least squares algorithms for modeling glucose metabolism in the human brain with corrections for vascular effects. Comput Methods Programs Biomed. 2002;68(1):1-14.

18. Patlak CS, Blasberg RG, Fenstermacher JD. Graphical evaluation of blood-to-brain transfer constants from multiple-time uptake data. J Cereb Blood Flow Metab. 1983;3(1):1-7.

19. Hallett WA. Quantification in clinical fluorodeoxyglucose positron emission tomography. Nucl Med Commun. 2004;25(7):647-50.

20. Vanzi E, Berti V, Polito C, et al. Cerebral metabolic rate of glucose quantification with the aortic image-derived input function and Patlak method: numerical and patient data evaluation. Nucl Med Commun. 2016;37(8):849-59.

21. Karakatsanis NA, Lodge MA, Tahari AK, Zhou Y, Wahl RL, Rahmim A. Dynamic whole-body PET parametric imaging: I. Concept, acquisition protocol optimization and clinical application. Phys Med Biol. 2013;58(20);7391.

22. Fang YH, Kao T, Liu RS, Wu LC. Estimating the input function non-invasively for FDG-PET quantification with multiple linear regression analysis: simulation and verification with in vivo data. Eur J Nucl Med Mol Imaging. 2004;31(5):692-702.

23. Chen K, Chen X, Renaut R, et al. Characterization of the image-derived carotid artery input function using independent component analysis for the quantitation of [18F] fluorodeoxyglucose positron emission tomography images. Phys Med Biol. 2007;52(23):7055-71.

24. Dai X, Chen Z, Tian J. Performance evaluation of kinetic parameter estimation methods in dynamic FDG-PET studies. Nucl Med Commun. 2011;32(1):4-16.

25. Marquardt D. An Algorithm for Least-Squares Estimation of Nonlinear Parameters. SIAM Journal on Applied Mathematics 1963;11(2):431–441.

26. Bailey DL, Townsend DW, Valk PE, Maisey MN. Positron Emission Tomography: Basic Sciences. Springer 2005.

27. Thompson HK Jr, Starmer CF, Whalen RE, McIntosh HD. Indicator transit time considered as a gamma variate. Circ Res. 1964;14:502-15.

28. Feng D, Huang SC, Wang X. Models for computer simulation studies of input functions for tracer kinetic modeling with positron emission tomography. Int J Biomed Comput. 1993;32(2):95-110.

29. Huang SC, Phelps ME, Hoffman EJ, Sideris K, Selin CJ, Kuhl DE. Noninvasive determination of local cerebral metabolic rate of glucose in man. Am J Physiol. 1980;238(1):E69-82.

30. Kuwabara H, Gjedde A. Measurements of glucose phosphorylation with FDG and PET are not reduced by dephosphorylation of FDG-6-phosphate. J Nucl Med. 1991;32(4):692-8.

31. Derdeyn CP, Videen TO, Yundt KD, et al.Variability of cerebral blood volume and oxygen extraction: stages of cerebral haemodynamic impairment revisited. Brain. 2002;125(Pt 3):595-607.

32. Ben Bouallègue F. A macroquantification approach for region-of-interest assessment in emission tomography. J Comput Assist Tomogr. 2013;37(5):770-82.

33. Rausch I, Cal-González J, Dapra D, et al. Performance evaluation of the Biograph mCT Flow PET/CT system according to the NEMA NU2-2012 standard. EJNMMI Phys. 2015;2(1):26.

34. Krejza J, Arkuszewski M, Kasner SE, et al. Carotid artery diameter in men and women and the relation to body and neck size. Stroke. 2006;37(4):1103-5.

35. Jovkar S, Evans AC, Diksic M, Nakai H, Yamamoto YL. Minimisation of parameter estimation errors in dynamic PET: choice of scanning schedules. Phys Med Biol. 1989;34(7):895-908.

36. Karakatsanis NA, Lodge MA, Casey ME, Zaidi H, Rahmim A. November. Impact of acquisition time-window on clinical whole-body PET parametric imaging. IEEE Nucl Sc Symp & Med Imag Conf (NSS/MIC). 2014.

37. Messa C, Choi Y, Hoh CK, et al. Quantification of glucose utilization in liver metastases: parametric imaging of FDG uptake with PET. J Comp Assist Tomogr. 1992;16(5); pp.684-69.

38. Karakatsanis NA, Zhou Y, Lodge MA, et al. Generalized whole-body Patlak parametric imaging for enhanced quantification in clinical PET. Phys Med Biol. 2015;60(22);8643-73.

39. Karakatsanis NA, Lodge MA, Zhou Y, et al. Novel multi-parametric SUV/Patlak FDG-PET whole-body imaging framework for routine application to clinical oncology. J Nucl Med. 2015;56(3);625-625.